

Wave Induced Wind in the Marine Boundary Layer

Øyvind Saetra*

The Norwegian Meteorological Institute, Oslo, Norway

Alvaro Semedo†

University of Uppsala, Uppsala, Sweden

Anna Rutgersson

University of Uppsala, Uppsala, Sweden

* *Corresponding author address:* Øyvind Saetra, The Norwegian Meteorological Institute, PO Box 43 Blindern, 0313 Oslo, Norway.

E-mail: Oyvind.Saetra@met.no

† *Also affiliated with:* National Laboratory for Sustainable Energy, Technical University of Denmark, Risø, Denmark

Abstract

Recent field observations and large-eddy simulations have shown that the impact of fast swell on the marine atmospheric boundary layer (MABL) might be stronger than previously assumed. For low to moderate winds blowing in the same direction as the waves, swell propagates faster than the mean wind. The momentum flux above the sea surface will then have two major components: the turbulent shear stress, directed downward, and the swell-induced stress, directed upward. For sufficiently high wave age values, the wave-induced component becomes increasingly dominant, and the total momentum flux will be directed into the atmosphere. Recent field measurements have shown that this upward momentum transfer from the ocean into the atmosphere has a considerable impact on the surface layer flow dynamics and on the turbulence structure of the overall MABL. The vertical wind profile will no longer exhibit a logarithmic shape, since an acceleration of the air flow near the surface will take place, generating a low level wave-driven wind maximum (a wind jet). As waves propagate away from their generation area as swell, some of the wave momentum will be returned to the atmosphere in the form of wave-driven winds.

A model that reproduces quantitatively and qualitatively the wave following atmospheric flow and the wave generated wind maximum, as seen from measurements, is proposed. The model assumes a stationary momentum and turbulent kinetic energy balance and uses the dampening of the waves at the surface to describe the momentum flux from the waves to the atmosphere. In this study, simultaneous observations of wind profiles, turbulent fluxes and wave spectra during swell events are presented and compared with the model. In the absence of an established model

for the linear damping ratio during swell conditions, we attempt to use the model combined with the observations to estimate the wave damping. For the cases where the observations showed a pronounced swell signal and almost no wind waves, the agreement between observed and modelled wind profiles are remarkably good. We find the resulting attenuation length relatively short, which suggests that the estimated damping ratios are too large. We attribute this, at least partly, to be caused by processes not accounted for by the model, such as the existence of an atmospheric background wind. In the model, this extra momentum must be supplied by the waves in terms of a larger damping ratio.

1. Introduction

Although it might seem intuitive that fast running waves (swell) arriving on light wind areas will have an impact on the local wind field, this concept had not been devoted the proper attention until the laboratory experiments by Harris (1966). During several experiments performed in an indoor wave tank, using a mechanical wave generator, it was noticed that a weak wind immediately above the waves was always present. Harris (1966) named this phenomenon the “wave-driven wind”.

Observations of the air-sea interaction regime in the presence of swell are relatively rare and sparse. Nevertheless studies in the early 1970s from different Soviet ocean campaigns (Volkov 1970; Belinov et al. 1974) and from Lake Michigan (Davidson and Frank 1973), from the Baltic Sea (Smedman et al. 1994, 1999; Rutgersson et al. 2001), and from several campaigns in the Atlantic and Pacific Oceans (Donelan et al. 1997; Grachev and Fairall 2001), have found evidence that the presence of fast running waves during light winds induces an upward momentum flux, directed from the water surface to the atmosphere.

The study from Smedman et al. (1999) was based on observations collected in the aftermath of a gale, from a tower located on the southern tip of the small island Östergarnsholm, east of Gotland Island in the Baltic Sea. During periods of strong swell regime, upward directed momentum fluxes were recorded from turbulence sensors. In addition, wind measurements at several levels showed a well defined negative wind gradient above the first measuring level (around 8 meters high above the mean sea level). This negative gradient indicated the presence of a low-level wind maximum in the lower marine atmospheric boundary layer (MABL). These findings were in agreement with what Harris (1966) had already postulated, saying that it would be possible that a wave-driven wind might produce a perturbation on the velocity profile by

increasing the wind velocity in the direction of wave propagation at low elevations above the water.

Until recently the wave-driven wind has been looked upon as a peculiarity or, as Grachev and Fairall (2001) mention, an exotic case. In spite of being an intriguing process, the dominant idea has been that it only occurs in a thin layer above the water surface, and that it has presumably no impact on the dynamics of the atmosphere (Janssen 2004). Sullivan et al. (2001) and Rutgersson and Sullivan (2005), using direct numerical simulations (DNS), and Sullivan et al. (2008), using large eddy simulations (LES), investigated the impact of swell on the MABL. Their findings indicate a stronger impact, in agreement with previous (Smedman et al. 1999) and more recent (Smedman et al. 2008) field measurements. The impact of swell was shown, both by measurements and simulations, not only to generate a wave-driven wind, but also to influence the overall turbulence structure of the MABL.

The basic concept behind the wave-driven wind and momentum transfer from the waves into the MABL, is that swell waves perform work on the overlying atmosphere as they propagate faster than the wind, producing a forward thrust on the flow. Hence swell loses momentum and energy to the atmosphere as it gradually decays, accelerating the airflow. Under swell influence, the wind profile exhibits a low-level wind maximum and a negative (or constant) gradient from there on, violating the logarithmic wind profile law. The Monin-Obukhov similarity theory cannot be claimed as valid in this situation (Miller et al. 1999; Smedman et al. 2008).

As Hristov et al. (2003) pointed out, the incomplete understanding of the atmosphere-ocean interchanging processes reduces the predictability not only of climate models, but also of weather and wave forecasting models. Swell is known to propagate thousands of kilometres across entire oceans (Snodgrass et al. 1966), crossing the tropics and the equatorial regions

where light wind regimes prevail. The picture that emerges from this feedback process is of momentum being transferred from the wind into the ocean at mid and high latitudes, where storms are more frequent. Part of this momentum is used in the wave generation process along storm tracks. As waves propagate away from their generation area as swell, some of this momentum is returned to the atmosphere, mainly at lower latitudes, in the form of wave-driven winds. Therefore a better physical understanding of this process is of considerable interest from a global climatological point of view.

Although the attenuation might be small, there is some decay in the swell energy as it propagates, and the physical mechanisms responsible for this attenuation remain poorly understood (Komen et al. 1994; Ardhuin and Jenkins 2006; Kantha 2006). A major question is how and where the wave energy is transferred, and how to model this air-ocean exchange process. Kudryavtsev and Makin (2004) presented numerical solutions from a one-dimensional stationary model for the MABL flow in the presence of swell. They have imposed an inner region and an outer region structure on the MABL, with the wave influence on the atmosphere being limited to the inner region. The model is conceptually based in the energy transfer from the waves to the atmosphere when the momentum flux is directed upward. Although in the situation where the wind is aligned with the swell propagating direction the model reproduces a low level wave-induced wind maximum, as found by Smedman et al. (1999) and Sullivan et al. (2008), the wind maximum is located at a lower height.

More recently Hanley and Belcher (2008) investigated how ocean waves affect the dynamics of the whole MABL by proposing different models of momentum budget above the ocean surface. The models were further used to assess the effect of swell on the wind profile and on the entire MABL dynamics. Their study was based on Ekman theory, modified by introducing

a wave-induced component on the total stress and on the Ekman wind profile. Besides qualitatively reproducing the LES experiment from Sullivan et al. (2008), they have proposed several criteria for the existence of swell driven wave-induced jets using different parameterizations of the eddy-viscosity coefficient and different turbulence closures, but like Kudryavtsev and Makin (2004), their study was not compared with field measurements.

In the present paper a model that reproduces qualitatively and quantitatively the wave-induced stress in the surface layer of the MABL wind is proposed. New parameterizations for the wave-induced stress at the surface (expressed as a function of the swell energy decay rate and wave slope), and variation with height are included in the model. The model results are compared with observations from a tower at the Östergarnsholm island, in the Baltic Sea.

In section 2, the measuring site and the data used in the comparisons are described. The selection criteria for the different cases used in the comparisons is also explained in this section. The model is derived in section 3, with two different parameterizations for the eddy viscosity (linearly varying with height and as a function of the turbulent kinetic energy). An extension of the model, where the assumption of constant total stress is relaxed is presented in the end of section 3. In section 4 some sensitivity tests and comparisons with wind speed profile observations are shown. In section 5 the results are discussed with reference to previous findings.

2. Observations

The measurements used in this study were taken at the Östergarnsholm site in the Baltic Sea. This air-sea interaction measuring site consists of an instrumented 30-m-high tower, situated at the southernmost tip of the island of Östergarnsholm (geographically located at $57^{\circ}27'N$ -

18°59'E) (see Fig. 1), and a Directional Wave rider Buoy (DWR). The DWR is run and owned by the Finish Institute of Marine Research (FIMR), and was moored about 4 km southwest of the tower where the water depth is 36 m. The island is very low and flat, with virtually no trees and very scarce vegetation. The tower base is located at 1 m above the mean sea level, with a +/- 0.5 m sea level variation.

High frequency Solent sonic 1012 anemometers (Gill instruments, Lymington, UK), mounted at 9, 16.5 and 25 m above the tower base, recorded turbulence data of the three wind components (and also temperature) at 20 Hz. In addition, slow response ("profile") sensors recorded wind speed and direction, and temperature, at 6.9, 11.8, 14.3, 20 and 28.8 m above tower base, at 1 Hz. A high-pass filter based on a 10-min linear detrending was applied to the turbulence time series to remove trends. Both turbulence and slow response data are 60-min averages. The wave measurements were recorded once every hour for 26 minutes long periods. The significant wave height was calculated using the integration trapezoidal method, from spectral frequencies between 0.025 and 0.58 Hz. The spectral variance, mean direction, directional spreading, skewness, and kurtosis were calculated over a frequency range of 68 bins from 0.025 to 0.58 Hz. For longer period waves (swell), which are the focus of this study, a wave transformation correction was applied (see appendix of Smedman et al. (1999)).

Both meteorological and wave data have been collected almost continuously since 1995 at this site. For the wind direction between (80° to 210° sector), the data has been shown to represent open sea conditions in the sense that the wave field is mainly undisturbed and the atmospheric turbulence is not influenced by the low water depths very near the shore (Högström et al. 2008a). Additional details about the measuring site, including the flux foot print analysis concept, and a detailed analysis about the wave field, the fetch conditions, and the bottom

topography in the vicinity of the buoy and around the southern shore of the island, can be found in Smedman et al. (1999, 2003) and Högström et al. (2008b).

The measurements used for the model comparisons in section 4 were obtained from two different periods: September 16-19, 1995, and September 22-23, 1996. A total of six cases were selected: four from the first period and two from the second.

Relatively low wind speeds were measured during the selected cases (indicating a light wind regime), and the wind direction was roughly aligned with the swell propagation direction. A swell dominated wave field was always present. In all the cases the 60-min averaged total momentum flux was negative, therefore directed upward. Relatively small positive heat fluxes were present, giving a slightly unstable stratification in both selected periods.

3. Model

Over the sea surface, when waves are present, the wind velocity has an additional component. Besides the mean and the turbulent components, found over land or rigid surfaces like ice, a wave-induced term is now present. The total kinematic stress (τ_{tot}) is therefore partitioned into turbulent shear stress (τ_{turb}), wave-induced stress (τ_{wave}) and viscous stress (τ_{visc}) (Phillips 1977):

$$\tau_{tot} = \tau_{turb} + \tau_{wave} + \tau_{visc}, \quad (1)$$

where the viscous component is neglected, since it is not important from a distance of the order of millimetres above the sea surface.

During the wave developing (or growing) process, the wave-induced stress (or wave-induced momentum flux) is directed downward, and is positive ($\tau_{wave} > 0$) (Komen et al. 1994). In this

situation energy and momentum are being supplied from the atmosphere to the sea surface. We define the wave age parameter as c_p/u_*

As waves start propagating away from their generation area the wave-induced momentum flux gradually decreases, reaches zero, and reverses sign, becoming negative ($\tau_{wave} < 0$) (Smedman et al. 1999; Grachev and Fairall 2001). When the wave-induced momentum flux becomes dominant over the turbulent stress (i.e. $|\tau_{wave}| > |\tau_{turb}|$), the total momentum flux will therefore reverse sign, becoming negative ($\tau_{tot} = \tau_{wave} + \tau_{turb} < 0$) and upward directed. The negative total momentum flux indicates that energy and momentum are being transferred from the sea surface to the atmosphere.

a. Constant flux model

A neutrally stratified MABL is considered. It is assumed that in the surface layer the effect of the Coriolis term is negligible, and therefore the total stress and its turbulent and wave-induced components are confined to the x -direction. For 2-dimensional stationary flow with no horizontal gradients, it follows from the principle of conservation of momentum that the shear stress is constant in the turbulent boundary layer:

$$\frac{d\tau_{tot}}{dz} = 0. \quad (2)$$

Here, z is the vertical coordinate, which is positive upward. The turbulent stress will be parametrised as

$$\tau_{turb} = K_m \frac{dU}{dz}, \quad (3)$$

where K_m is the turbulent eddy viscosity and U is the mean horizontal wind. Inserting (3) in equation (2) yields an equation for the mean horizontal wind:

$$\frac{dU}{dz} = \frac{\tau_{tot} - \tau_{wave}}{K_m}. \quad (4)$$

The wave stress is

$$\tau_{wave} = - \langle \tilde{u}\tilde{w} \rangle, \quad (5)$$

where u and w are the longitudinal and vertical components of the flow. The brackets indicate time averaging the tilde denote wave-induced flow fluctuations.

A parametrisation for τ_{wave} nevertheless is still needed. For irrotational waves, the orbital velocity components decay as e^{-kz} , where k is the wave number. In this case, the vertical and horizontal components are 90 degrees out of phase. The wave stress is then of course zero. When a small amount of work is performed at the surface, the velocity components are slightly phase shifted, as observed in the Large Eddy Simulations (LES) of Sullivan et al. (2008). Their findings indicate an exponentially decaying with height wave-induced stress, in agreement with prior numerical calculations presented by Chalikov and Belevich (1993), and with the field measurements of Högström et al. (2008b). In this study it will be assumed that the upward directed wave-induced stress will have the form

$$\tau_{wave} = \tau_{wave}^0 e^{-2kz}, \quad (6)$$

where τ_{wave}^0 is the wave-induced stress at the surface.

This surface wave stress can be related to the energy damping through the rate of work performed at the surface. For one harmonic wave component, the energy per unit area is

$$E = \frac{1}{2} \rho_w g a^2, \quad (7)$$

where ρ_w is the water density, g is the acceleration of gravity and a is the wave amplitude. The rate of change of wave energy caused by a surface stress is proportional to the phase velocity times the stress:

$$\frac{\partial E}{\partial t} = \rho_a c \tau_{wave}^0, \quad (8)$$

where c is the phase velocity. By linear theory, the rate of change of wave energy in decaying waves may be written as

$$\frac{\partial E}{\partial t} = \beta E, \quad (9)$$

where β is the growth rate or the wave damping coefficient depending on the sign. Using equations (7), (8) and (9), the relation between τ_{wave}^0 and β is found to be

$$\tau_{wave}^0 = \frac{1}{2} \frac{\beta g a^2}{s c}, \quad (10)$$

where $s = \rho_a / \rho_w$. By substituting this in equation (6), the wave stress can be written as

$$\tau_{wave} = \frac{1}{2} \frac{\beta g a^2}{s c} e^{-2kz}. \quad (11)$$

For a wave spectrum, the wave stress is found by adding the contribution from all wave components:

$$\tau_{wave} = \int_0^\infty \frac{\beta g S(f)}{s c} e^{-2kz} df. \quad (12)$$

Here, $S(f)$ is the wave spectrum and f is the frequency. In this case, β is positive in the high frequency range and changes sign for long waves travelling faster than the wind. If we define β^g as the growth rate and β^d as the damping coefficient, the wave stress can be rewritten as

$$\tau_{wave} = \int_0^{f_c} \frac{\beta^d g S(f)}{s c} e^{-2kz} df + \int_{f_c}^\infty \frac{\beta^g g S(f)}{s c} e^{-2kz} df. \quad (13)$$

f_c is the frequency corresponding to a wave phase speed equal to the 10 metre wind speed .

This frequency can be seen as a separation between the swell and the young sea parts of the

wave spectra, and is

$$U_{10} = c = \frac{\omega}{k} = \frac{g}{\omega} = \frac{g}{2\pi f_c} \Rightarrow f_c = \frac{g}{2\pi U_{10}} \quad (14)$$

where $\omega = \sqrt{gk}$ is the angular frequency for deep water waves and U_{10} is the wind speed at 10 meters.

The eddy viscosity can be related to the turbulent kinetic energy, b , and the mixing length, l , as

$$K_m^b = l\sqrt{b}. \quad (15)$$

In this study a neutral stratification is assumed and the mixing length will be taken to be

$$l = \kappa z, \quad (16)$$

where $\kappa = 0.4$ is the von Karman constant. Following Kudryavtsev and Makin (2004), we assume a balance between shear production, vertical rate of change of energy flux and dissipation of turbulent kinetic energy. The turbulent kinetic energy budget is then (Tennekes and Lumley 1972)

$$\tau_{tot} \frac{dU}{dz} + F_w - \epsilon = 0. \quad (17)$$

where ϵ is the energy dissipation. The wave term in equation (17) is

$$F_w = -\frac{1}{\rho_a} \frac{d}{dz} (\langle \tilde{p}\tilde{w} \rangle). \quad (18)$$

Here, \tilde{p} is the fluctuating part of the pressure due to the waves and ρ_a is the density of the air.

The energy dissipation term is often parametrised as

$$\epsilon = \frac{b^{3/2}}{l}. \quad (19)$$

Combining equations (3), (15), (17) and (19) yields an equation for the turbulent kinetic energy,

$$b^2 = |\tau_{tot}(\tau_{tot} - \tau_{wave}) + l\sqrt{b}F_w|. \quad (20)$$

Here, the total stress can be negative, i.e upward directed. This will be the case whenever the magnitude of the wave stress is larger than the turbulent stress. The shear production term in equation (17) may therefore become negative. The absolute value of the first term on the right hand side is taken to avoid negative production of turbulent kinetic energy.

The energy flux in equation (20) is related to the rate of work:

$$- \langle \tilde{p}\tilde{w} \rangle = -\rho_a c \langle \tilde{u}\tilde{w} \rangle \Rightarrow - \langle \tilde{p}\tilde{w} \rangle = \rho_a c \tau_{wave}^0 e^{-2kz}. \quad (21)$$

Accordingly, the pressure perturbation term for in (20) for one harmonic component becomes

$$F_w = -2k c \tau_{wave}^0 e^{-2kz}. \quad (22)$$

For a wave spectrum the expression can be written as

$$F_w = - \int_0^{f_c} \frac{2\beta^d g k S(f)}{s} e^{-2kz} df - \int_{f_c}^{\infty} \frac{2\beta^g g k S(f)}{s} e^{-2kz} df. \quad (23)$$

If the damping and growth rates are known, the wave stress and wave energy flux can be calculated from equations (13) and (23). The wind profile is then found by solving equations (4) and (20) numerically. Using a prescribed eddy viscosity instead of equation (20) yields a simplified solution that nicely illustrate the general behaviour of the model. For this purpose we will use an eddy viscosity that is varying linearly with height. Strictly, this is only valid in the absence of waves. However, as the eddy viscosity will have to increase with height near the surface we will assume that the assumption of a linearly increasing eddy viscosity does not violate the general structure of the solution. It will be presented here to demonstrate how the traditional boundary layer model is modified in the presence of swell. The eddy viscosity is then taken to be:

$$K_m^l = \kappa z u_*. \quad (24)$$

Here, $u_* = \sqrt{|\tau_{tot}|}$ is the friction velocity. Using equation (11) for the wave stress, the solution to equation (4) is

$$U(z) = \frac{\tau_{tot}}{\kappa u_*} \ln\left(\frac{z}{z_0}\right) - \frac{\tau_{wave}^0}{\kappa u_*} \int_{z_0}^z \frac{e^{-kz}}{z} dz, \quad (25)$$

where z_0 is the aerodynamic roughness length. In the absence of wave stress, equation (25) reduces to the well known logarithmic profile. We see that the introduction of the wave stress yields a new term that modifies the traditional logarithmic distribution. For cases when the total stress is upward directed, the logarithmic term is negative while the wave term becomes a production term for mean wind in the MABL.

b. Non-constant flux model

The assumption of a constant momentum flux in the surface MABL allows for relatively broad variations with height: up to 10% of its magnitude over the all surface layer (Stull 1988). Recent field campaigns have collected observations that do not confirm the constant flux assumption under a swell dominated wave field. The total momentum flux magnitude has been observed to decrease with height (Smedman et al. 2008). This decrease in magnitude is related to the impact of swell on the turbulence structure in the MABL. The starting point is the fact that swell induces modifications in the turbulence production mechanism close to the surface. These modifications have an impact on the turbulence structure and dynamics of the entire MABL, and are expected to drive the non-constant momentum flux, breaking one of the assumptions of the Monin-Obukhov similarity theory. Assuming that τ_{tot} is no longer constant, but varies linearly with height, tending asymptotically to values close to zero outside the surface MABL:

$$\tau_{tot} = \tau_{tot}^0 + \alpha z, \quad (26)$$

where τ_{tot}^0 is the value of the flux at the surface and α its vertical gradient, which is assumed to be constant and positive, so that the magnitude of τ_{tot} is actually decreasing. Following the same steps that lead to equation (25), the wind speed profile then becomes

$$U(z) = \frac{\tau_{tot}}{\kappa u_*} \ln\left(\frac{z}{z_0}\right) - \frac{\tau_{wave}^0}{\kappa u_*} \int_{z_0}^z \frac{e^{-kz}}{z} dz + \frac{\alpha}{\kappa u_*} (z - z_0). \quad (27)$$

An additional term is present on the right-hand side. This term will determine the departure from the original wind speed profiles due to the vertical the variation of the total momentum flux. The impact of the non-constant momentum flux MABL will be explored in greater detail in the following section.

4. Results

a. General behaviour of the model

In this section general model results, along with some model sensitivity tests, are presented. The behaviour of the wind speed profiles from equations (25) and the numerical solution of (4) and (20), corresponding the linearly varying with height eddy-viscosity K_m^l , and to the TKE dependent eddy-viscosity K_m^b , respectively, are investigated. The input parameters to the model are an upward directed constant momentum flux $\tau_{tot} = -10^{-2} m^2 s^{-2}$, a wave damping parameter $\beta = -5 \times 10^{-5} s^{-1}$, and a constant roughness length $z_0 = 10^{-5} m$. We stress that these values have been chosen only to demonstrate the overall behaviour. The realistic values will be discussed in more detail later. The monochromatic wave field is assumed to have a wave amplitude $a = 1m$ and a wave number $k = 0.1 m^{-1}$, corresponding to a wave phase speed $c = 9.9 m s^{-1}$, a wave period $T \approx 6.3 s$ and wave length $L \approx 63 m$.

The two wind speed profiles, corresponding to the two eddy-viscosity formulations, are

shown in Fig 2. A distinctive wave-induced low-level wind jet (or wind maximum) in the surface MABL, for both eddy-viscosities, can be seen in Fig 2a. The wind profile calculated using the K_m^l eddy-viscosity (dashed line) has a more pronounced bulge, and higher wind speed at the wind maximum (jet strength), compared with the profile evaluated with the K_m^b eddy-viscosity (dot-dashed line). The heights of the wind maxima are the same for both cases ($z \approx 3$ m). The wind speeds at the jet are 3.6 m s^{-1} and 2.5 m s^{-1} , for the K_m^l and K_m^b eddy-viscosities, respectively. Fig. 2b shows the two wind speed profiles for the entire MABL, normalised by the background flow U_B . The height of the boundary layer is assumed to be 200 metres, and the background flow the wind speed at that height. The wave induced wind speed departures from U_B at low levels can be seen for both eddy-viscosity formulations. Above the jet the wind speed reduces smoothly to the background flow in both profiles. This feature is in qualitative agreement with the LES predictions from Sullivan et al. (2008).

The vertical profiles for the two eddy-viscosities are shown in Fig. 3. The inclusion of the TKE on the K_m^b formulation gave rise to an increase of the eddy viscosity up to about 25 meters, compared with the linearly varying K_m^l formulation. The immediate result is a vertical diffusion of momentum. This turbulence diffusion leads to a less pronounced wind jet, as seen in Fig. 2a. The lower jet strength is also related to the momentum diffusion.

An additional horizontal wind speed profile from equation (27), with the K_m^l eddy-viscosity, is shown in Fig. 4. The input parameters remained unchanged, with the exception of the total stress that is now decaying (in magnitude) with height according to equation (26), where $\tau_{tot}^0 = -0.01 \text{ m}^2 \text{ s}^2$ and $\alpha = 3 \times 10^{-4} \text{ m s}^{-2}$. The surface MABL height, where the total stress eventually becomes zero, and the TKE vanishes, is assumed to be 30 metres. The decrease in magnitude of τ_{tot} resulted in an increase of the wind speed at higher levels, and to a less

enhanced jet (dashed line), when compared with the original wind speed profile computed with a constant total momentum flux (full line).

The vertical profiles of the total stress and its components, the turbulent and wave-induced stresses, used as input parameters, are showed in Fig 5. In Fig. 5a, τ_{tot} is constant with height (vertical full line), τ_{wave} (dashed line) is evaluated from equation (11), and the turbulent stress (dot-dashed line) is computed from $\tau_{turb} = \tau_{tot} - \tau_{wave}$. The vertical profiles of the stresses resulting from the non-constant stress model are shown in Fig 5b, where $\tau_{tot} \approx \tau_{turb} \approx 0$ at $z = 30 \text{ m}$. The less pronounced bulge is due to the decrease (in magnitude) of τ_{turb} after a certain height, tending to a decreasing τ_{tot} . The characteristics of the wind profiles in Fig. 2 are related to the stresses profiles shown in Fig 5a, and to the dynamical processes behind them. Bellow the jet the wind speed gradient is positive. In this layer the wave-induced stress accelerates the wind because there is a significant amount of momentum being transferred from the waves to the atmosphere; the turbulent stress is positive (and downwards). At the height of the jet τ_{turb} is zero, and reverses sign and direction from there up (becoming negative and upward), corresponding to a smoother negative wind speed gradient. The physical sense of this process is in agreement with the LES results from Sullivan et al. (2008), and with the field observations and findings of Högström et al. (2008b).

Model sensitivity tests to the variability of the wave damping parameter, and the roughness length, using the model formulation from equation (25), are performed. The model response to the variations of β^d is shown in Fig. 6. The original profile with $\beta^d = -5 \times 10^{-5} \text{ s}^{-1}$ is shown as a full line. The wave damping parameter is then slightly varied ($\Delta\beta^d = \pm 3 \times 10^{-6} \text{ s}^{-1}$), keeping all the remaining parameters unchanged. Increased values of β^d , corresponding to a larger loss of energy from the waves into the atmosphere, lead to a stronger jet and higher jet (wind profiles

in dashed lines in Fig 6). The opposite effect, with lower values of β^d , and consequently less energy transfer from the waves, lead to a weaker and lower jet. The horizontal shift of the wind profiles on Fig. 6 occurs due to the fact that only β^d is varied and all the remaining parameters are kept unchanged.

The fact that the wind profile over the ocean, under swell conditions, is no longer logarithmic makes the correct evaluation of the roughness length a cumbersome problem (Smedman et al. (2003), their Figs. 3 and 7). For the model sensitivity tests to roughness length variations several formulations are used (Table 1). Once again the original profile evaluated with $z_0 = 10^{-5} m$ is kept as a reference, and is shown as a full line in Fig. 7. The profiles corresponding to several roughness lengths from the different formulations are shown as dashed lines. The effect of roughness length variations is different than the one obtained with the variations of the damping parameter β^d . The impact is no longer caused only by the wave-induced part of equation (25), but also by the logarithmic component of the profile. Variations of z_0 have an impact on the wind speed only, and not on the height of the wind speed maxima, as can be seen in Fig 6. Larger values of z_0 give rise to lower wind speed values, and reduced z_0 values to higher wind speeds. The sensitivity of the model to the roughness length is, however, relatively small. The wave age dependent relation roughness length from Smith (1992), $z_0 = 0.48u_*^2/g(u_*/c_p)^{1.0}$, will be used in the model comparisons with observations in the following section.

b. Comparisons with field measurements

In the present section the modelled wind profiles from equation (25) and the numerical solution of the equations (4) and (20), corresponding to the K_m^l and K_m^b eddy-viscosities, are compared with wind speed measurements from the 30 m high tower at Östergarnsholm Island.

The observed input parameters to the modelled wind profiles are the total stress form highest measuring level, the roughness length, the wave amplitude and the wave phase speed. The wave amplitude is approximated by one half of the observed significant wave height ($a \approx H_s/2$). Due to the relatively small heat fluxes measured in the tower (not shown here), a neutrally stratified surface MABL is assumed.

From all the needed input parameters, the one that has not been observed is the wave attenuation/growth parameter β . A clear conclusion about the parameterizations of the parameter β is still lacking, on both the growth and the decaying regimes (but particularly on the latter), as Hanley and Belcher (2008) describe. As far as our knowledge goes, there is no study or measurements available in the open literature describing specifically the damping rate of swell aligned with the wind. There are some laboratory studies on wave energy attenuation, but they are mainly focused on the effect of an opposing aligned wind on wave energy decay (Donelan 1999; Pierson et al. 2003). The results from these laboratory experiments are not consensual, and most of the times are either not in agreement with the theory or cannot be directly applied in the open ocean (Kudryavtsev and Makin 2004).

Ardhuin and Jenkins (2006) concluded that, besides losing energy to the atmosphere, swell also transfers energy to the ocean mixed layer. The loss of energy from swell into the ocean occur when waves and upper ocean turbulence co-exist, and the interaction between the two leads to a transfer of energy from waves to TKE. They have also concluded that for swell propagating in the wind direction, the transfer of wave energy into the ocean is at least one order of magnitude smaller than the loss of energy to the atmosphere.

The lack of a proper parametrisation for the parameter β makes the comparisons of the model wind profiles proposed in the present study with field observations rather challenging.

Instead of using one of the proposed parameterizations available in the literature, the wind speed observations from the tower are used as an input to the model. By using the formulation for the total (net) wave-induced stress in equation (13), the damping parameter, β^d , is then taken as a residual parameter by forcing both modelled profiles to go through the observed wind speed at the lowest level. For that purpose we introduce the weighted average of the damping parameter over the low frequency range of the observed wave energy spectra $\widehat{\beta}^d$ such that

$$\tau_{wave} = \widehat{\beta}^d \int_{f_{min}}^{f_c} \frac{gS(f)}{sC} e^{-2kz} df + \int_{f_c}^{f_{max}} \frac{\beta^g gS(f)}{sC} e^{-2kz} df, \quad (28)$$

where f_{min} and f_{max} are the minimum and maximum frequency in the observed spectra. The frequency f_c is computed by using an interpolated U_{10} between the two lowest wind speed observation levels. In a similar way the wave term in equation (20) is calculated as

$$F_w = -\widehat{\beta}^d \int_{f_{min}}^{f_c} \frac{2gkS(f)}{s} e^{-2kz} df - \int_{f_c}^{f_{max}} \frac{2\beta^g gkS(f)}{s} e^{-2kz} df. \quad (29)$$

For the young sea part of the wave spectra, the growth of the waves remained frequency dependent, and assumed to be explained by the parametrisation from Belcher and Hunt (1993):

$$\beta^g = C_\beta \omega s \left(\frac{u_*}{c} \right)^2, \quad (30)$$

where C_β is a constant, ω is the wave frequency in radians. Following Hanley and Belcher (2008) the wave growth-rate coefficient is taken as $C_\beta = 0.32$. The observed 1-D wave energy density spectra are used as an input for computing the total (net) wave-induced stress and the wave energy flux from equations (28) and (29).

As mentioned in section 2, the selection of the six cases had as main a priori condition an upward directed momentum flux (60-min averaged), followed by the conditions established in Högström et al. (2008a) for the so called swell cases at the footprint area of the Östergarnsholm measuring site. The six cases are ordered chronologically and are designated from A to F.

Although being a limitation that the lowest wind speed measuring level is as high as 7.9 metre, the fact that from this level up the wind profiles in all cases exhibit a well defined negative gradient, allows the plausible speculation that a wind speed maxima will be somewhere between this level and the surface (Smedman et al. 1999).

Figs. 8 and 9 show the comparisons between observed wind speeds (black squares joined by full line) and modelled wind speed profiles computed for the six cases (dashed and dot-dashed lines for the K_m^l and K_m^b eddy-viscosities, respectively). The observed wave energy spectra for each case are also shown in Figs. 8 and 9. The wave spectra are divided in two parts by a dashed vertical line. This line separates the swell energy part from the young seas part, being the separation frequency f_c .

There is a very good qualitative and quantitative agreement between the observed and the modelled wind speed profiles in cases A, B, C, and F, with not so good agreement in cases D and E. The quality of the agreement between the observed and modelled profiles seems to be directly related to the wave age parameter, here defined as c_p/u_* . All cases are clearly swell dominated, since for all of them $c_p/u_* > 20$. Nevertheless the lowest wave age values, indicating a less swell dominated wave field, are the ones measured during cases D and E, whereas for cases A, B, C, and F the wave age values are higher. The values of the total stress, damping ratios, amplitudes, wave lengths and attenuation lengths are listed in Table 2.

In cases A, B, C and F, the wave damping parameter $\widehat{\beta}^d$ is consistently of the order of $-10^{-4} s^{-1}$ for both modelled profiles. The exception are cases A and B (only for the K_m^l eddy-viscosity) where the values (magnitude) are slightly smaller ($-\widehat{\beta}^d = 0.89 \times 10^{-4} s^{-1}$ and $-\widehat{\beta}^d = 0.69 \times 10^{-4} s^{-1}$, for cases A and B, respectively). The values for cases D and E are one order of magnitude higher for both eddy-viscosities. The values of the damping parameter $\widehat{\beta}^d$

for all cases are listed in Table 2. The inverse wave age plotted against $\widehat{\beta}^d$ is shown in Fig. 10. There is a clear decrease in $|\widehat{\beta}^d|$ as the inverse wave age (or as the swell dominance) decreases, in agreement with Kudryavtsev and Makin (2004).

The height of the jet was evaluated for all cases for both eddy-viscosities. The height is higher in the profiles evaluated with the K_m^b eddy-viscosity, when compared with the ones evaluated with the K_m^l eddy-viscosity. The reason relies on momentum diffusion, as before. The difference between the height on the modelled profiles is relatively more pronounced (1-2 metres) for the cases A,B,C, and F, compared to the cases D and E (~ 0.5 metres). On these two last cases height of the jet was also lower. The justification for this lower height can be the possible disruption of the wind-driven jet by the presence of a background flow, or, just with the poor agreement these two cases show when compared with the observations. On the other hand, assuming that the effect of an unaccounted background flow is very small on cases A, B, C and F, the wind speed maxima at heights 4-6 metres can be assumed to be driven (mostly) by the upward directed momentum flux from the waves, and therefore closer to reality.

The spatial scale of attenuation can be calculated as

$$L_a = c_g/|\beta^d|, \quad (31)$$

where c_g is the group velocity, approximated for the peak wave speed as $c_g \approx c_p/2$. The results are listed in Table 2. The values seems to be rather small even when considering the relatively short wave lengths in these observations (also in Table 2), indicating that the damping ratios are too large. The wave lengths ranges from 20 to 48 metres with attenuation lengths from 98 kilometres down to almost 6 kilometres for some cases. We see that the longest, and probably closest to realistic, attenuation lengths are found for the cases A to C. These are also the cases with best agreement in the comparison between the modelled and the observed wind

distribution. We believe that the too large damping ratios can be explained by background wind not accounted for in the model. If a background wind exist during the observations, the model must adjust for this by an artificially large momentum flux, and hence a too large damping ratio. The model is very sensitive to the values of τ_{tot} . Uncertainties in the measured total momentum flux might also have contributed for such high tuned values of the damping ratios. An additional source of error that can be held accounted is the fact that a neutrally stratified MABL is assumed. As seen in the LES by Sullivan et al. (2008), the effect of buoyancy in the dynamics of a swell dominated MABL can be considerable.

5. Conclusions

The effect of fast running waves on the overlaying MABL is stronger than it has been assumed until recently, as seen from the LES predictions in Sullivan et al. (2008), and in the recent field measurements in Smedman et al. (2008) and Högström et al. (2008b). A swell dominated wave field is frequently in a state of disequilibrium in light wind conditions, and loses momentum and energy to the overlaying atmospheric flow as it propagates. In this situation the net momentum and energy exchange over the air-sea interface changes direction and are directed upwards to the atmosphere. The most striking effect of this process is the flow acceleration in the lower surface MABL, leading to the formation of a low level wind jet. Nevertheless the effect of swell is not constrained to the surface, since it can be extended to the all MABL, by changing its vertical turbulence structure up to the top.

In this paper a model for the effect of swell on the wind profile in the surface layer of the MABL is described. The model is based on the swell loss of energy into the atmosphere, quan-

tified by the wave damping parameter. The governing parameter behind the model is the form drag, here proposed as a function of the wave energy loss, and the wave field characteristics. The wave-induced stress is assumed to decay exponentially with height, in agreement with Sullivan et al. (2008) LES results, and with Högström et al. (2008b) findings, for swell dominated wave fields. Two mixing length closure schemes are used for the eddy viscosity: one assuming a linear variation with height and the second assuming a dependence on TKE, governed by the wave energy flux. The model assumes a swell dominated wave field and a net upward directed transport of momentum, so that at the surface the wave-induced stress dominates over the turbulent stress. Although measurements of such situations are scarce and difficult to obtain, they have been observed over the ocean and are one of the key assumption behind the LES in Sullivan et al. (2008). The observations used in the model comparisons with field measurements had to meet this criterion.

The proposed model reproduces the characteristics and the dynamics of the surface layer of a swell dominated MABL for wind following waves, in agreement with the findings of Sullivan et al. (2008), and Högström et al. (2008b), and also with prior field observations, mainly from Smedman et al. (1994, 1999). The comparisons with field measurements show a good agreement between modelled and measured wind speed profiles. This agreement is especially good for the cases with high wave age parameter, indicating a predominant wave effect in the surface MABL. The wave damping parameter is treated as a residual term, by forcing the modelled profiles to fit the observed wind speed at the lowest level in the tower. Furthermore, the weighted average of the damping parameter over the swell part of the spectrum is calculated to allow for the wave spectra balance between the swell and the wind waves.

The attenuation length is calculated from the damping ratio and the group velocity. We

obtained attenuation lengths shorter than 100 kilometres. Swell is known to propagate over considerable distances so these attenuation lengths seems indeed to be small. Accordingly, the damping ratios must be too large. One possible explanation is the existence of a background wind not accounted for in the model. In the model, such additional momentum must be supplied by the waves, yielding artificially large damping ratios. The fact that the cases with clearest swell signals gave the largest attenuation lengths supports this hypothesis. This argument also explains the poor qualitative fitting of the modelled profiles in cases D and F. In all the six cases the observed damping decreases with decreasing inverse wave age. This behaviour also suggests that the proposed parametrisation of the form drag reflects the reality.

Since the lowest observation level was 8.6 metres, the height of the jet was not measured but inferred to be below that level, due to the observed negative wind gradient from that level up. Therefore comparisons between modelled and observed jet heights and strengths are not possible. Nevertheless the results obtained with the model, with both eddy viscosity formulations, for cases A, B, C and F, can be viewed as close to reality, if compared with the observations (Smedman et al. 2008; Högström et al. 2008b), where a similar swell dominated wave field was present. The rather extreme wave field characteristics imposed in the LES in Sullivan et al. (2008) do not allow for a quantitative comparison as far as the jet strength and height are concerned.

Both a linearly varying eddy viscosity and an eddy viscosity calculated from the TKE budget lead the model to reproduce the effect of swell on the surface MABL. In view of the values obtained for wave damped parameter and for the swell attenuation length, the results based on a linearly varying eddy viscosity produced smaller, and hence more realistic, values of the wave damping parameter. Since the effect of the wave energy flux in the TKE budget in the lowest

meters, below the height of the jet, cannot be ignored, this issue should be further explored in future work.

The driving parameter that ultimately determines the effect of fast running waves in the MABL is the swell energy rate of change. Only extensive field measurements of this parameter along with the effect of swell waves in the lower atmosphere, preferably in open ocean, can contribute to improve our knowledge this effect.

Acknowledgments.

This research was partly funded by The Research Council of Norway through the project ArcChange, contract 178577/S30, and IPY-THORPEX, contract 175992/S30. The contribution from Alvaro Semedo was funded by the European Commission through a research fellowship under the ModObs project, contract MRTN-CT-2005-019369. We like to thank Professor Jan Erik Weber, Professor Ulf Högström and Professor Ann-Sofi Smedman for support and valuable discussions. The wave observations were kindly provided by Dr. Heidi Pettersson and Dr. Kimmo Kahma.

References

- Ardhuin, F. and A. D. Jenkins, 2006: On the interaction of surface waves and upper ocean turbulence. *J. Phys. Oceanogr.*, **36**, 551–557.
- Belcher, S. E. and J. C. R. Hunt, 1993: Turbulent shear flow over slowly moving waves. *J. Fluid Mech.*, **251**, 109–148.
- Belinov, A. Y., O. A. Kuznetsov, and G. N. Panin, 1974: On the analysis of wind-wave induced disturbances in the atmospheric turbulent surface layer. *Bound. Layer Meteor.*, **6**, 269–285.
- Chalikov, D. V. and M. Y. Belevich, 1993: One-dimensional theory of the boundary layer. *Bound. Layer Meteor.*, **63**, 65–96.
- Charnock, H., 1955: Wind stress on a water surface. *Quart. J. Roy. Meteor. Soc.*, **81**, 639–640.
- Davidson, K. L. and A. J. Frank, 1973: Wave-related fluctuations in the airflow above natural waves. *J. Phys. Oceanogr.*, **3**, 102–119.
- Donelan, M., 1990: *The Sea*, chap. Air-Sea interaction, 239–292. Willey-Interscience, New York.
- Donelan, M. A., 1999: *Wind-over-wave couplings*, chap. Wind-induced growth and attenuation of laboratory waves, 183–194. Calderon Press.
- Donelan, M. A., W. M. Drennan, and K. B. Katsaros, 1997: The air-sea momentum flux in conditions of wind sea and swell. *J. Phys. Oceanogr.*, **27**, 2087–2099.

- Grachev, A. A. and C. W. Fairall, 2001: Upward momentum transfer in the marine boundary layer. *J. Phys. Oceanogr.*, **31**, 1698–1710.
- Hanley, K. E. and S. E. Belcher, 2008: Wave-Driven Wind Jets in the Marine Atmospheric Boundary Layer. *J. Atmos. Sci.*, **65** (8), 2646–2660.
- Harris, D. L., 1966: The wave-driven wind. *J. Atmos. Sci.*, **23**, 688–693.
- Högström, U., E. Sahlée, W. M. D. K. K., Kahma, A.-S. Smedman, C. Johansson, H. Pettersson, A. Rutgersson, L. Tuomi, F. Zhang, and M. Johansson, 2008a: Momentum fluxes and wind gradients in the marine boundary layer a multi platform study. *Accepted in Boreal Env. Res.*, **00**, 00–00.
- Högström, U., A.-S. Smedman, E. Sahlée, W. M. Drennan, K. K. Kahma, C. Johansson, H. Pettersson, , and F. Zhang, 2008b: The atmospheric boundary layer during swell - a field study of the governing mechanism. *Submitted to J. Atmos. Sci.*, **00**, 00–00.
- Hristov, T. S., S. D. Miller, and C. A. Friehe, 2003: Dynamical coupling of wind and ocean waves through wave-induced air flow. *Nature*, **422**, 55–58.
- Janssen, P., (Ed.) , 2004: *The Interaction of Ocean Waves and Wind*. Cambridge University Press.
- Kantha, L., 2006: A note on the decay rate of swell. *Ocean Modelling*, **11**, 167–173.
- Komen, G. J., L. Cavaleri, M. Doneland, K. Hasselmann, S. Hasselmann, and P. A. E. M. Janssen, (Eds.) , 1994: *Dynamics and Modelling of Ocean Waves*. Cambridge University Press.

- Kudryavtsev, V. N. and V. K. Makin, 2004: Impact of swell on the marine atmospheric boundary layer. *J. Phys. Oceanogr.*, **34**, 934–948.
- Miller, S., C. Friehe, T. Hristov, J. Edson, and S. Wetzel, 1999: *Wind-over-wave couplings*, chap. Wind and turbulent profiles in the surface layer over ocean waves, 91–98. Calderon Press.
- Phillips, O. M., (Ed.) , 1977: *The dynamics of the upper ocean*. Cambridge University Press.
- Pierson, W. L., A. W. Garcia, and S. E. Pells, 2003: Water wave attenuation due to opposing wind. *J. Fluid Mech.*, **487**, 345–365.
- Rutgersson, A., A.-S. Smedman, and U. Höglström, 2001: Use of conventional stability parameters during swell. *J. Geophys. Res.*, **106**, 27 117–27 134.
- Rutgersson, A. and P. P. Sullivan, 2005: The effect of idealized water waves on the turbulence structure and kinetic energy budgets in the overlying airflow. *Dyn. Atmos. Oceans*, **38**, 147–171.
- Smedman, A., X. g. Larsén, U. Höglström, K. K. Kahma, and H. Pettersen, 2003: Effect of sea state on the momentum exchange over the sea during neutral conditions. *J. Geophys. Res.*, **108**, 1–13.
- Smedman, A., U. Höglström, H. Bergström, A. Rutgersson, K. K. Kahma, and H. Pettersen, 1999: A case study of air-sea interaction during swell conditions. *J. Geophys. Res.*, **104**, 25 833–25 851.
- Smedman, A., U. Höglström, E. Sahleé, W. M. Drennan, K. K. Kahma, H. Pettersson, and

- F. Zhang, 2008: Observational study of marine atmospheric boundary layer characteristics during swell. *Submitted to J. Atmos. Sci.*
- Smedman, A., M. Tjernström, and U. Högström, 1994: The Near-Neutral Marine Atmospheric Boundary Layer with No Surface Shearing Stress: A Case Study. *J. Atmos. Sci.*, **51**, 3399–3411.
- Smith, S. D., 1992: Sea surface wind stress and drag coefficients: The hexos results. *Bound. Layer Meteor.*, **60**, 109–142.
- Snodgrass, F. E., G. W. Groves, K. F. Hasselmann, G. R. Miller, W. H. Munk, and W. H. Powers, 1966: Propagation of Ocean Swell across the Pacific. *Phil. Trans. Roy. Soc. London*, **259A**, 431–497.
- Stull, R. B., 1988: *An Introduction to Boundary Layer Meteorology*. Academic Publishers, Dordrecht.
- Sullivan, P. P., J. B. Edson, T. Hristov, and J. C. McWilliams, 2008: Large-eddy Simulations and Observations of Atmospheric Marine Boundary Layers above Nonequilibrium Surface Waves. *J. Atmos. Sci.*, In press.
- Sullivan, P. P., J. C. McWilliams, and C.-H. Moeng, 2001: Simulation of turbulent flow over idealized water waves. *J. Fluid Mech.*, **404**, 47–85.
- Tennekes, H. and J. L. Lumley, 1972: *A first course in turbulence*. MIT Press, Cambridge.
- Volkov, Y. A., 1970: Turbulent flux of momentum and heat in the atmospheric surface layer over a disturbed sea-surface. *Izv. Acad. Sci. USSR, Atmos. Ocean. Phys. (Engl. Transl.)*, **6(12)**, 734–770.

List of Figures

1	Map of the Baltic Sea, with a close-up of the measuring site. The wave buoy is moored at ~ 4 kilometres east-southeast of the tower in the island, at 36 metres deep water.	35
2	Wind speed profiles for both eddy-viscosity formulations: K_m^l (dashed line), and K_m^b (dot-dashed line) at the surface MABL (a). The triangle and the diamond represent the wind speed maxima, for the K_m^l (dashed line) and K_m^b eddy-viscosities, respectively. Normalised wind speed profiles for both eddy-viscosity formulations (b), with the boundary layer depth being 200 metres. The thin horizontal line represents the x-axis.	36
3	Eddy-viscosities profiles: K_m^l (dashed line) and K_m^b (dot-dashed line). The thin horizontal and vertical lines represent the x-axis and y-axis, respectively.	37
4	Wind speed profiles for constant and non-constant total stress models. The full line is the wind speed profile for K_m^l eddy-viscosity, with a constant total stress, as in Fig. 2. The dashed (dot-dashed) line is the departure from the full line wind speed profile, due to a decreasing with height total momentum flux. The triangle represents the wind speed maximum. The thin horizontal line represents the x-axis.	38

- 5 Profiles of the total momentum flux, wave-induced stress, and turbulent stress, for the constant stress model (a) and non-constant stress model (b). The full thick line is the total momentum, negative (upward directed), and constant with height. The dashed line is the wave-induced stress, negative (upward directed), and tending asymptotically with height to zero ($\tau_{wave} \rightarrow 0$). The dot-dashed line is the turbulent stress, positive (downward directed), and negative (upward directed), tending asymptotically with height to the total stress ($\tau_{turb} \rightarrow \tau_{tot}$). The thin horizontal line represents the x-axis. 39
- 6 Model sensitivity tests to the variability of the wave damping parameter β^d . The full line is the wind speed profile for the K_m^l eddy-viscosity, as in Fig. 2. The dashed line wind speed profiles are the result of variations in the wave damping parameter ($\Delta\beta^d = \pm 3 \times 10^{-6} s^{-1}$). The black triangle symbols represent the wind speed maxima. The height of the wind speed maxima decreases for decreasing values of β^d . The thin horizontal and vertical lines represent the x-axis and y-axis, respectively. 40

- 7 Model sensitivity tests to the variability of the aerodynamic roughness length . The full line is the wind speed profile for the eddy-viscosity, as in Fig. 2, with computed from the Charnock (1955) relation. The dashed line wind speed profiles are the result of variations in the roughness length due to different formulations. The symbols represent the wind speed maxima corresponding to each formulation: the circle to Kudryavtsev and Makin (2004), the triangle smooth flow, the pentagram to Donelan (1990), and the square to Smith (1992). Lower (higher) values of lead to higher (lower) wind speed maxima. The thin horizontal and vertical lines represent the x-axis and y-axis, respectively. 41
- 8 Comparisons between observed and modelled wind speed profiles, for both eddy viscosities (left column, a, c and e), and wave spectra (right column, b, d, and e) for cases A, B, and to C. The dashed line profiles correspond to the K_m^l eddy-viscosity, and the dot-dashed line profiles are the K_m^b eddy-viscosity. The triangles and the diamonds represent the wind speed maxima. The squares represent the observed wind speeds in the tower. The dotted vertical line in the wave spectra represents the separation between the swell and young seas components of the spectra. 42
- 9 Comparisons between observed and modelled wind speed profiles, for both eddy viscosities (left column, g, i, and l), and wave spectra (right column, h, j, and m) for cases D, E, and F. (Remaining legend as in Fig. 8.) 43

10 Observed swell damping rate as a function of inverse wave age The triangles and the diamonds represent the wave age vs. the damping ratio. for the K_m^l and the K_m^b eddy-viscosities, respectively. The dashed (dot-dashed) line is a fit for the two eddy-viscosities. 44

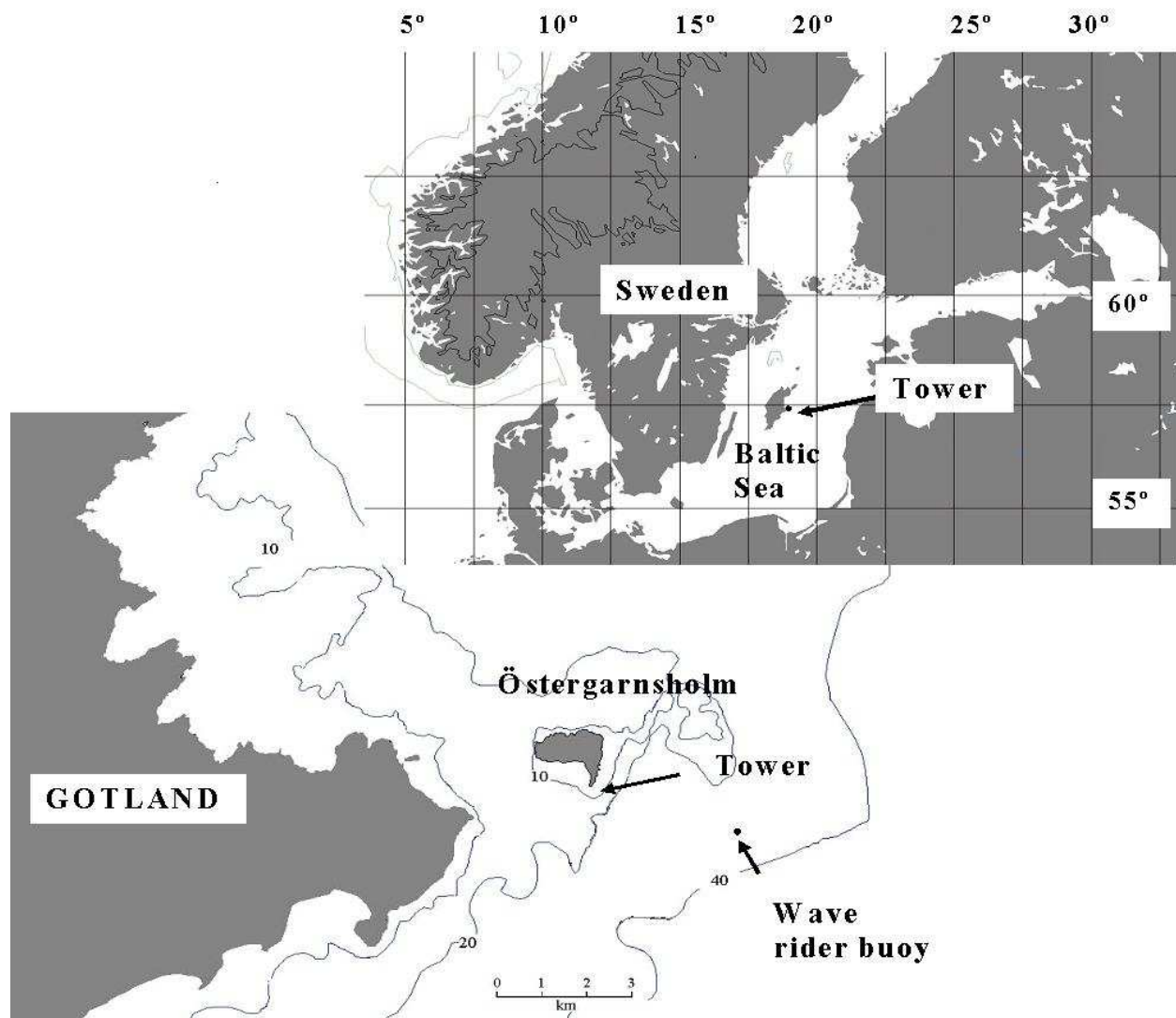


FIG. 1. Map of the Baltic Sea, with a close-up of the measuring site. The wave buoy is moored at ~ 4 kilometres east-southeast of the tower in the island, at 36 metres deep water.

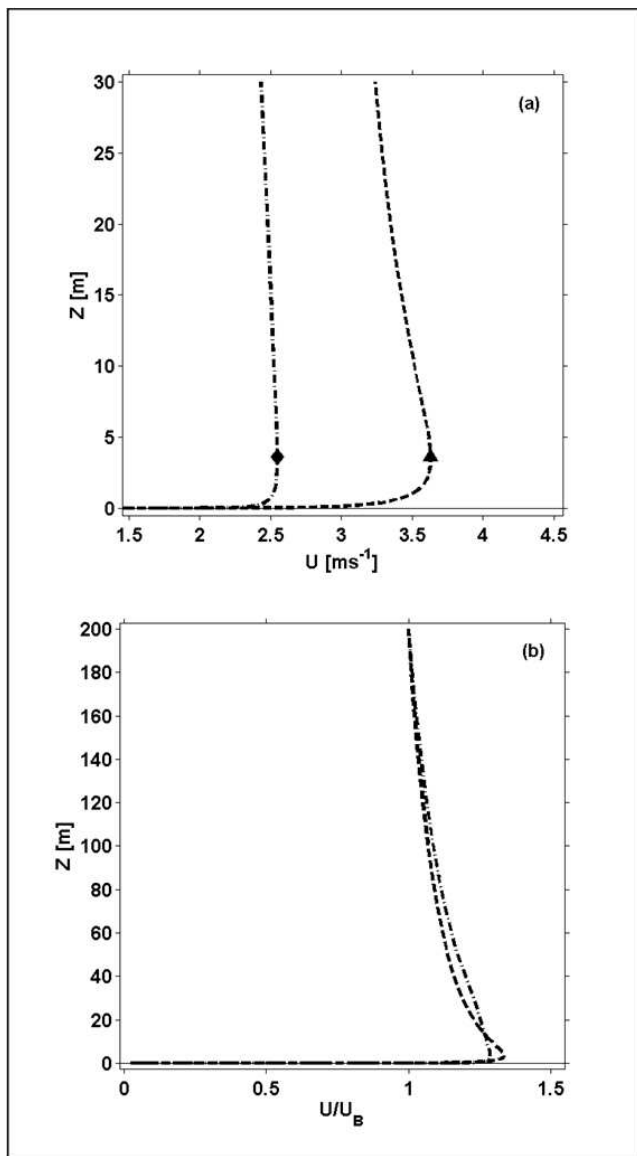


FIG. 2. Wind speed profiles for both eddy-viscosity formulations: K_m^l (dashed line), and K_m^b (dot-dashed line) at the surface MABL (a). The triangle and the diamond represent the wind speed maxima, for the K_m^l (dashed line) and K_m^b eddy-viscosities, respectively. Normalised wind speed profiles for both eddy-viscosity formulations (b), with the boundary layer depth being 200 metres. The thin horizontal line represents the x-axis.

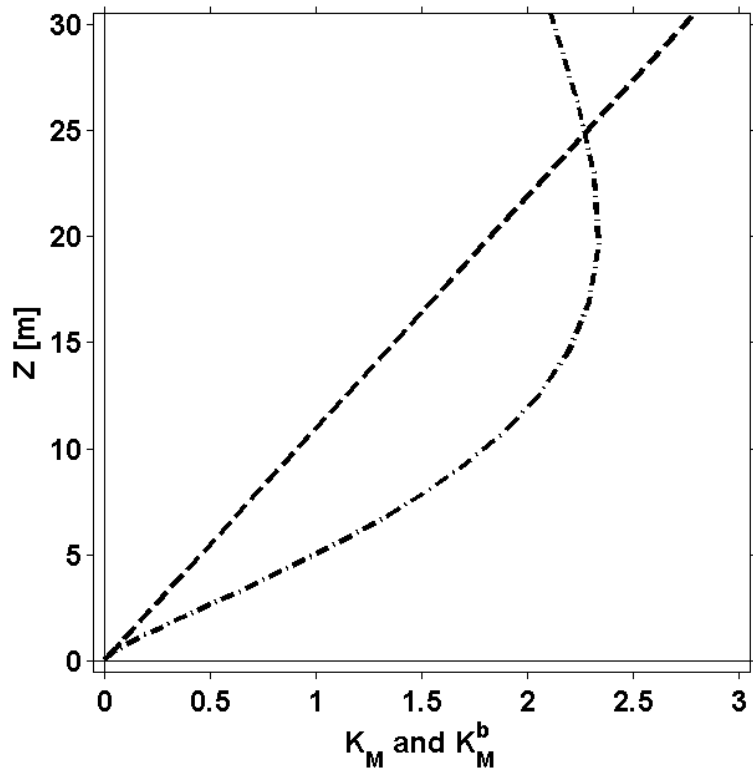


FIG. 3. Eddy-viscosities profiles: K_m^l (dashed line) and K_m^b (dot-dashed line). The thin horizontal and vertical lines represent the x-axis and y-axis, respectively.

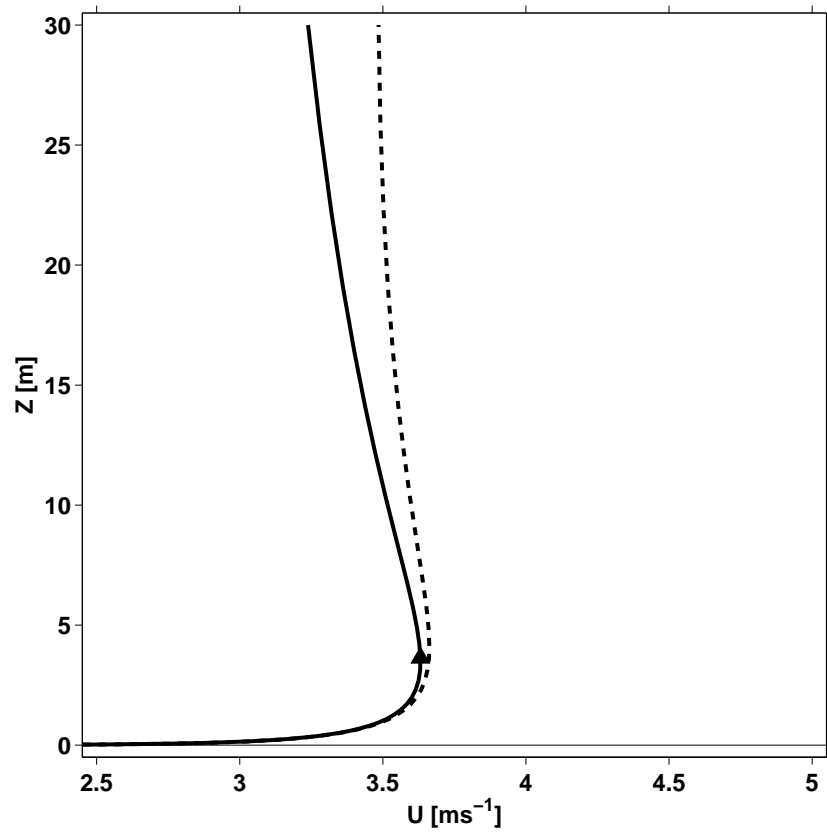


FIG. 4. Wind speed profiles for constant and non-constant total stress models. The full line is the wind speed profile for K_m^l eddy-viscosity, with a constant total stress, as in Fig. 2. The dashed (dot-dashed) line is the departure from the full line wind speed profile, due to a decreasing with height total momentum flux. The triangle represents the wind speed maximum. The thin horizontal line represents the x-axis.

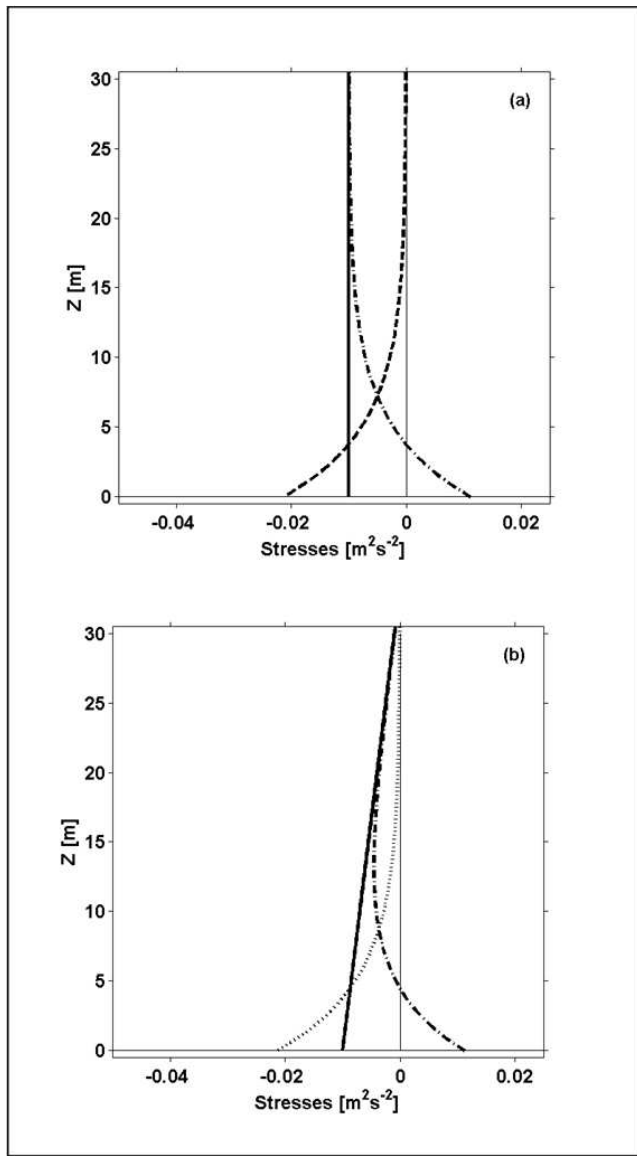


FIG. 5. Profiles of the total momentum flux, wave-induced stress, and turbulent stress, for the constant stress model (a) and non-constant stress model (b). The full thick line is the total momentum, negative (upward directed), and constant with height. The dashed line is the wave-induced stress, negative (upward directed), and tending asymptotically with height to zero ($\tau_{wave} \rightarrow 0$). The dot-dashed line is the turbulent stress, positive (downward directed), and negative (upward directed), tending asymptotically with height to the total stress ($\tau_{turb} \rightarrow \tau_{tot}$). The thin horizontal line represents the x-axis.

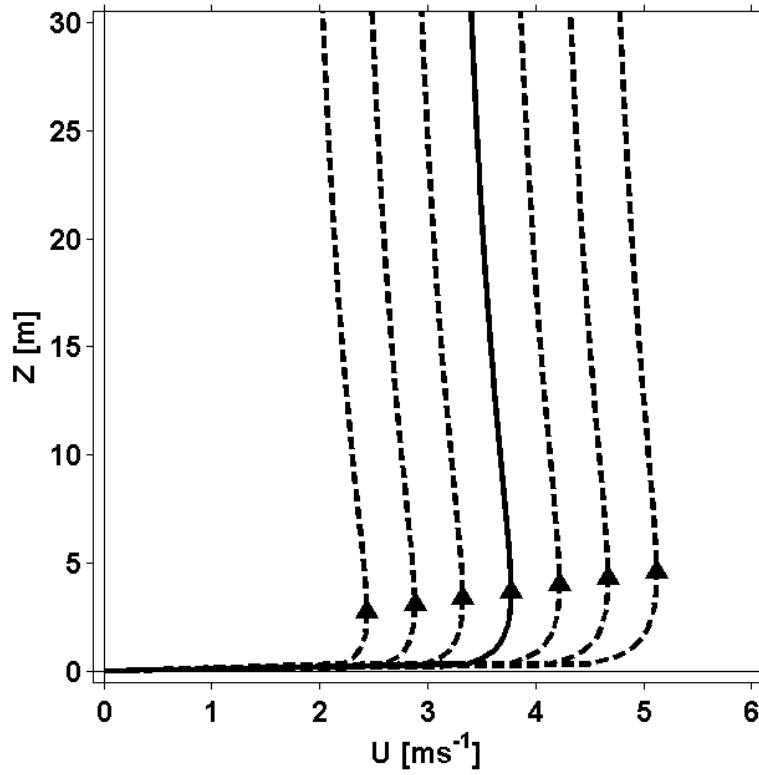


FIG. 6. Model sensitivity tests to the variability of the wave damping parameter β^d . The full line is the wind speed profile for the K_m^l eddy-viscosity, as in Fig. 2. The dashed line wind speed profiles are the result of variations in the wave damping parameter ($\Delta\beta^d = \pm 3 \times 10^{-6} \text{ s}^{-1}$). The black triangle symbols represent the wind speed maxima. The height of the wind speed maxima decreases for decreasing values of β^d . The thin horizontal and vertical lines represent the x-axis and y-axis, respectively.

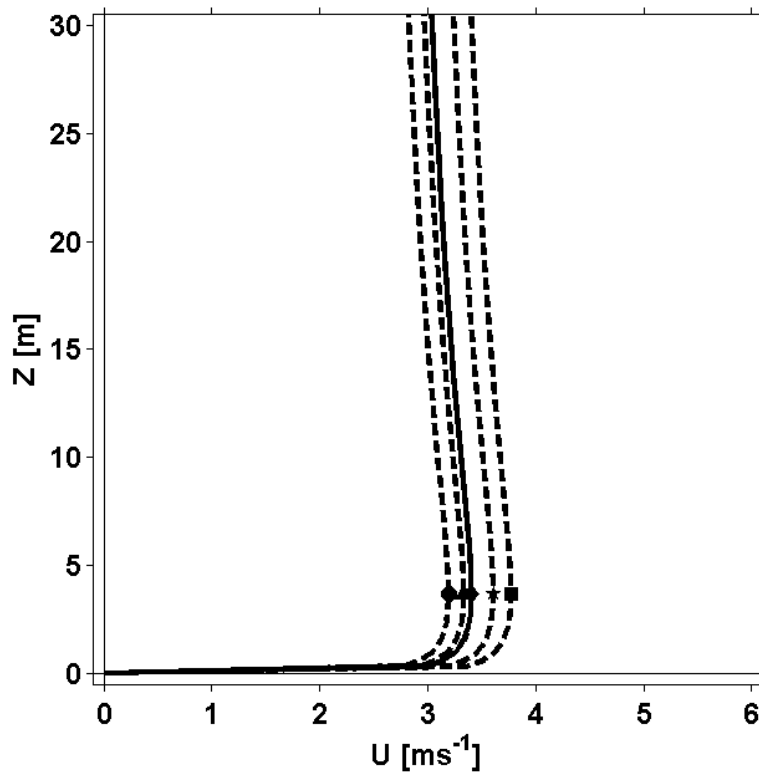


FIG. 7. Model sensitivity tests to the variability of the aerodynamic roughness length . The full line is the wind speed profile for the eddy-viscosity, as in Fig. 2, with computed from the Charnock (1955) relation. The dashed line wind speed profiles are the result of variations in the roughness length due to different formulations. The symbols represent the wind speed maxima corresponding to each formulation: the circle to Kudryavtsev and Makin (2004), the triangle smooth flow, the pentagram to Donelan (1990), and the square to Smith (1992). Lower (higher) values of lead to higher (lower) wind speed maxima. The thin horizontal and vertical lines represent the x-axis and y-axis, respectively.

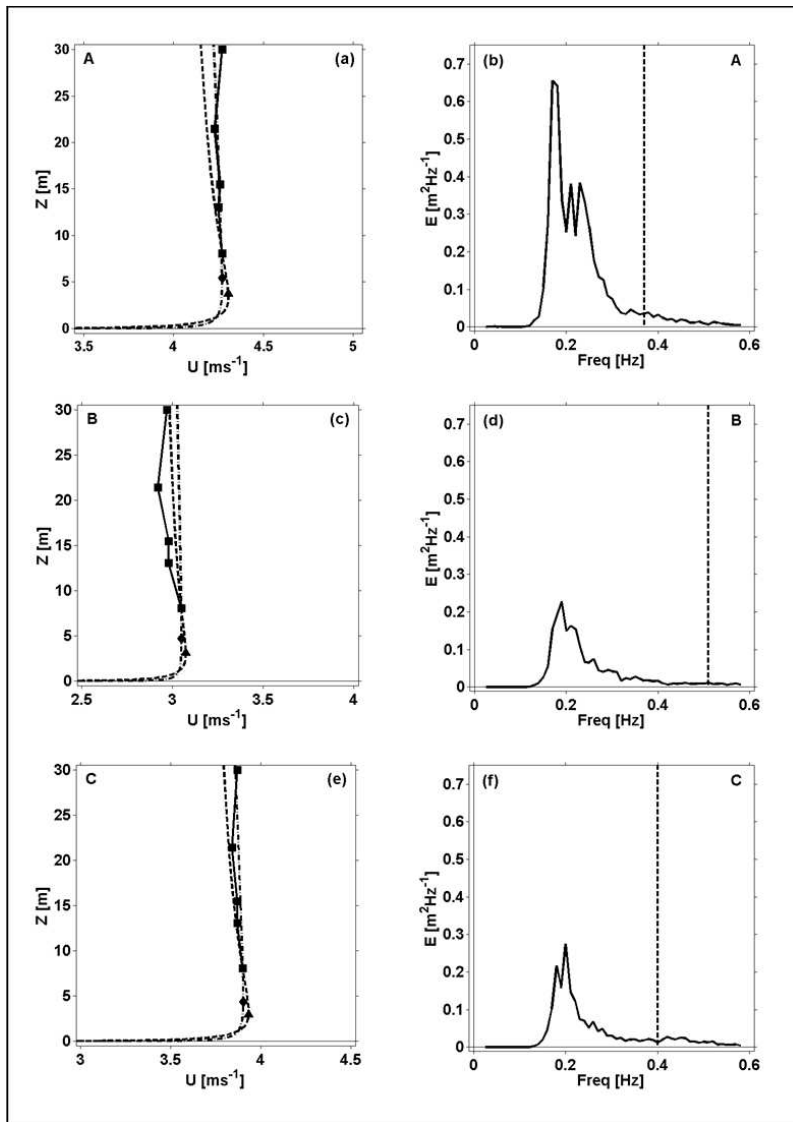


FIG. 8. Comparisons between observed and modelled wind speed profiles, for both eddy viscosities (left column, a, c and e), and wave spectra (right column, b, d, and e) for cases A, B, and to C. The dashed line profiles correspond to the K_m^l eddy-viscosity, and the dot-dashed line profiles are the K_m^b eddy-viscosity. The triangles and the diamonds represent the wind speed maxima. The squares represent the observed wind speeds in the tower. The dotted vertical line in the wave spectra represents the separation between the swell and young seas components of the spectra.

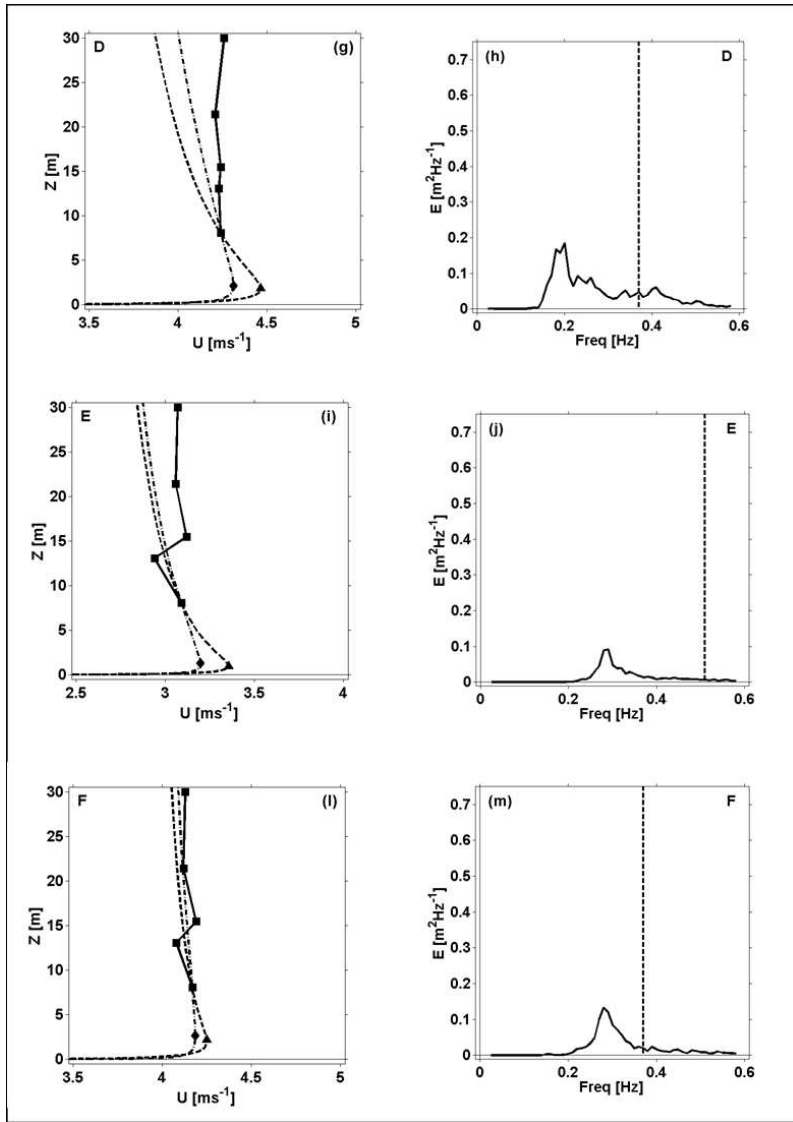


FIG. 9. Comparisons between observed and modelled wind speed profiles, for both eddy viscosities (left column, g, i, and l), and wave spectra (right column, h, j, and m) for cases D, E, and F. (Remaining legend as in Fig. 8.)

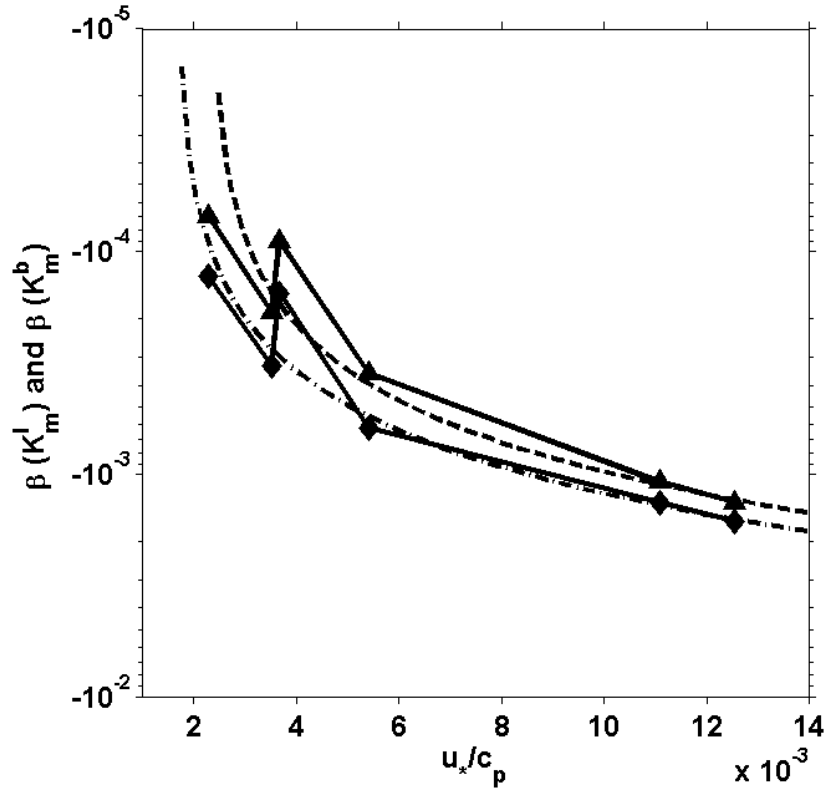


FIG. 10. Observed swell damping rate as a function of inverse wave age. The triangles and the diamonds represent the wave age vs. the damping ratio for the K_m^l and the K_m^b eddy-viscosities, respectively. The dashed (dot-dashed) line is a fit for the two eddy-viscosities.

List of Tables

1	Aerodynamic roughness length (z_0) formulations.	46
2	Observed input parameters and tuned damping parameter for the two eddy viscosity formulations.	47
3	Modelled wind speed maxima (U_{max}) and height of the maxima (z_{max}) for the K_m^l and K_m^l eddy viscosity formulations.	48

TABLE 1. Aerodynamic roughness length (z_0) formulations.

Reference	Formulation
Kudryavtsev and Makin (2004)	$z_0 = 0.1\nu/u_* + 0.012u_*^2/g$
Smooth flow	$z_0 = 0.11\nu/u_*$
Charnock (1955)	$z_0 = 0.012u_*^2/g$
Donelan (1990)	$z_0 = 1.84\sigma(u_*/c_p)^{2.53}$
Smith (1992)	$z_0 = 0.48u_*^2(u_*/c_p)$

TABLE 2. Observed input parameters and tuned damping parameter for the two eddy viscosity formulations.

Cases	τ_{tot}	K_m^l	K_m^b	a	λ	c_p/u_*	K_m^l	K_m^b
		$\widehat{\beta}^d$	$\widehat{\beta}^d$				L_a^l	L_a^b
	$(10^{-3}m^2s^{-2})$	$(10^{-3}m^2s^{-2})$	$(10^{-4}s^{-1})$	(m)	(m)	1	(km)	(km)
A	-1.22	-0.90	-1.54	0.43	48	271.8	81	44
B	-0.38	-0.70	-1.29	0.28	39	438.3	98	50
C	-0.93	-1.87	-3.26	0.30	40	284.5	48	26
D	-11.28	-13.5	-16.3	0.31	38	79.7	7.4	5.9
E	-4.88	-10.9	-13.4	0.19	21	90.3	6.3	5.0
F	-11.08	-3.52	-6.20	0.21	20	185.1	19	11

TABLE 3. Modelled wind speed maxima (U_{max}) and height of the maxima (z_{max}) for the K_m^l and K_m^b eddy viscosity formulations.

Cases	K_m^l		K_m^b	
	U_{max} (m/s)	z_{max} (m)	U_{max} (m/s)	z_{max} (m)
A	4.28	4.50	4.27	6.61
B	3.06	3.81	3.05	5.78
C	3.92	4.36	3.90	5.30
D	4.41	2.50	4.27	2.92
E	3.30	1.30	3.16	1.81
F	4.25	2.18	4.19	3.17